



Membrane distillation against a pressure difference

L. Keulen^{a,1}, L.V. van der Ham^b, N.J.M. Kuipers^c, J.H. Hanemaaijer^c, T.J.H. Vlught^a,
S. Kjelstrup^{a,d,*}



^a Department of Process and Energy, Delft University of Technology, Leeghwaterstraat 39, 2628CB Delft, The Netherlands

^b Department of Process and Instrument Development, Netherlands Organisation for Applied Scientific Research, TNO, 2628CA Delft, The Netherlands

^c Department of Water Treatment, Netherlands Organisation for Applied Scientific Research, TNO, 3704HE Zeist, The Netherlands

^d Department of Chemistry, Norwegian University of Science and Technology, NTNU, NO-7491 Trondheim, Norway

ARTICLE INFO

Keywords:

Membrane distillation
Water desalination
Heat and mass transfer
MemPower
Irreversible thermodynamics

ABSTRACT

Membrane distillation is an attractive technology for production of fresh water from seawater. The MemPower® concept, studied in this work, uses available heat (86 °C) to produce pressurized water (2.2 bar and 46 °C) by membrane distillation, which again can be used to power a turbine for co-production of electricity. We develop a non-equilibrium thermodynamic model to accurately describe the transfer at the liquid-membrane interfaces, as well as through the hydrophobic membrane. The model can explain the observed mass flux, and shows that 85% of the energy is dissipated at the membrane-permeate interface. It appears that the system's performance will benefit from a lower interface resistance to heat transfer, in particular at the permeate side of the membrane. The nature of the membrane polymer and the pore diameter may play a role in this context.

1. Introduction

Fresh drinking water is essential for life on earth. We need water to survive, not only as drinking water, but also in food production, washing, industry, etc. According to the United Nations, the increase in potable water use was more than twice the rate of the population increase in the last century [1]. By 2025, an estimated 1.8 billion people will live in areas with water scarcity, and two-thirds of the world's population will be living in water-stressed regions as a result of water use, growth and climate change [1]. New solutions are therefore needed to decrease the scarcity of clean water in the world. Nearly 70% of the earth is covered by water, but only 2.5% of that water is fresh and usable for consumption, and only 1% of the fresh water is easily accessible [2]. The rest is trapped in glaciers or snowfields.

Consequently, fresh water produced from seawater and brackish water becomes increasingly important. Between 1% and 2% of the fresh water used as drinking or process water, is extracted from brackish and saline water [3]. In 2006, the desalination capacity worldwide was 40 million m³/day [3]. In 2011 it had increased to almost 70 million m³/day [3]. Many desalination processes exist, for example multi-stage flashing, multi-effect distillation, reverse osmosis, electro-dialysis or membrane distillation. The driving forces for these processes are either thermal, osmotic or electrical. The challenge in all cases is to obtain reasonable energy input and equipment costs per amount of

fresh water produced.

Membrane distillation (MD) is attractive in this context, because of its possibility to use low grade waste heat as energy source in the production of drinking water. The first publication on MD dates back to the sixties of the last century [4]. Water vapor is transported through a membrane, driven by a temperature difference. The membrane pores are filled with water vapor, in contrast to other techniques, where water is transported in the liquid phase. Presently, MD is nearly commercial. The technology is competitive with reverse osmosis for low heat costs and feedstock with high osmotic pressures. The possibility to fully understand and possibly improve the attractive MD process has motivated the present study of a new invention, namely the MemPower® process concept [3,5–8]. Fig. 1 provides a schematic illustration of the MemPower concept [8], when used for seawater desalination. It produces fresh water against a hydrostatic pressure difference with the help of a thermal driving force. An aqueous feedstock with hydrostatic pressure $P_{\text{total},2}$ (e.g. seawater) is first heated to temperature T_2 , e.g. by utilizing low grade heat. During normal operation, water is transported against a pressure difference, $P_{\text{total},3} - P_{\text{total},2}$, due to the transport of the latent heat of water down the temperature gradient. The positive temperature difference, $T_2 - T_3$, can be said to drive the desalination process, producing distilled water on the permeate side. The figure to the right shows the pressure of the distillate, $P_{\text{total},3}$, maintained by throttling of the effluent valve on this

* Corresponding author at: Department of Chemistry, Norwegian University of Science and Technology, NTN, NO-7491 Trondheim, Norway

E-mail addresses: luuc.keulen@polimi.it (L. Keulen), signe.kjelstrup@ntnu.no (S. Kjelstrup).

¹ Current affiliation: Department of Aerospace Science and Technology, Politecnico di Milano, 20156 Milano, Italy.

Nomenclature

B	membrane permeability, $\text{m}^2\text{K J/K mol s}$
c_w	concentration of water, mol/m^3
D_w	Fick's diffusion coefficient for water vapor, m^2/s
d	thickness, m
H_j	molar enthalpy of component j , J/mol
$H_{j,T}$	molar enthalpy of component j at temperature T , J/mol
$\Delta H_{\text{vap},j}$	enthalpy of evaporation of component j , J/mol
J	general symbol for flux
J_j	flux of component j , mol/s m^2
J_q	thermal energy flux, J/s m^2
J'_q	measurable heat flux, J/s m^2
k_B	Boltzmann constant, $1.3807 \cdot 10^{-23} \text{ kg m}^2/\text{s}^2 \text{ K}$
L	mean free path, m
\dot{m}	mass flow, kg/s
M_j	molar mass of component j , kg/mol
n	number of borders between control volumes, dimensionless
N	number of control volumes, dimensionless
P	total pressure, N/m^2
P_w^*	vapor pressure of water at saturation, N/m^2
q	heat of transfer, J/mol
r_{mn}	local resistivity coefficient, coupling force m to flux n
R	universal gas constant, 8.3145 J/K mol
R^{tot}	resistivity matrix for global description of system
T	absolute temperature, K
x	coordinate axis for transport, m
X_i	general symbol for driving force no i

Greek symbols

$\Delta_{\text{ab}} Y$	difference in property Y : $Y_b - Y_a$
λ	thermal conductivity, J/s K m^2
μ_j	chemical potential of component j , J/mol
$\mu_{j,T}$	chemical potential of component j at temperature T , J/mol
σ	local entropy production, J/K m^3 or J/K m^2
ε	membrane porosity, dimensionless
Ω	membrane cross-sectional area, m^2

Sub- and superscripts

0	reference point or ideal gas state
a,b,c,d	points on the x -axis
CV	control volume
i,j	component indices
h	homogeneous face
k	control volume index
l	liquid
mem	membrane
per	permeate
q	thermal energy or measurable heat
ret	retentate
s	interface
T	temperature
tot	total
vap	vapor
w	water

side. The pressure $P_{\text{total},3}$ is larger than the hydrostatic pressure on the feed side $P_{\text{total},2}$, meaning that water transport takes place against a pressure difference. It is indicated in the concept, Fig. 1 on the left, that the pressurized distillate can be used to drive a turbine to generate hydroelectric power. The power density is the turbine efficiency times the pressure difference and the volumetric flow of distillate. The net

effect of this, is that (waste) heat can be used to produce drinking water as well as hydroelectric power. The process will continue until an upper pressure, the so-called break-through pressure of the membrane, is reached. At this pressure, the pores become wetted, causing liquid water to flow back via the membrane from the distillate to the feed.

Typical temperature and pressure variations under operation are

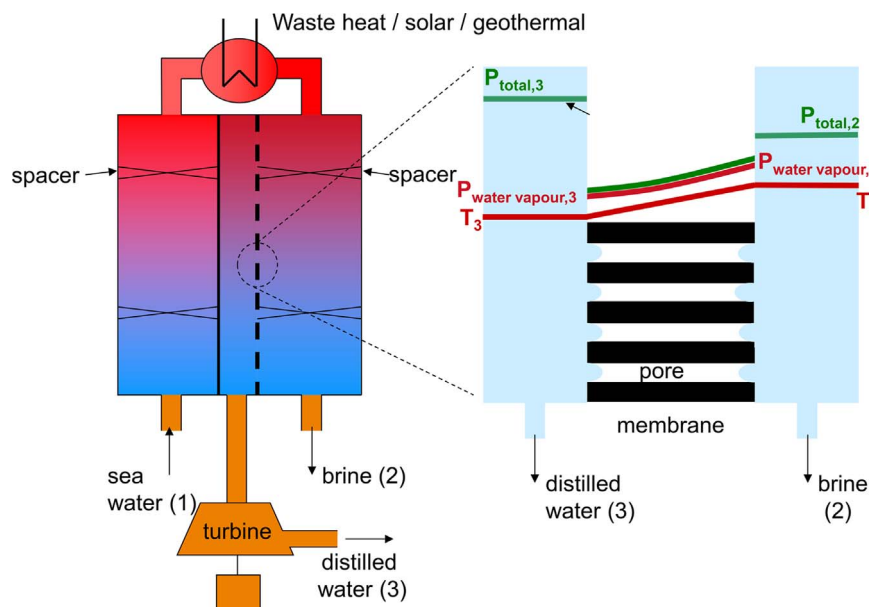


Fig. 1. Schematic representation of the MemPower concept [8] as applied to seawater desalination. Cold seawater enters the feed side, at (1) to the left in the figure, and flows through a compartment with non-permeable walls, where it is preheated by a counter-currently flowing stream at the permeate side. The preheated seawater is further heated by an external heat source, which can be waste heat from the industry, solar or geothermal energy. The heated seawater enters the retentate side of the system (2) with pressure $P_{\text{total},2}$, where the water will partially evaporate and pass through membrane pores to the permeate side, at (3) in the figure, due to the temperature difference $T_3 - T_2$. The permeate compartment is shown in the center of the figure to the left, as well as in the enlargement to the right hand side figure. The water vapor condenses to yield distilled water at the permeate side at the hydrostatic pressure $P_{\text{total},3}$. The distilled water is heated by the latent heat freed by condensation and heat conducted via the membrane material.

schematically illustrated in the right-hand side of Fig. 1. Present state-of-the-art modeling is not able to compute the pressure variation from the temperature variation. This is because simple fluxes of mass and heat are used (Fick's and Fourier's law) [9,10]. The heat and mass fluxes are then regarded as independent of one another, a problem mentioned by some authors [11,12]. The liquid-vapor surface resistivities on both membrane sides are also neglected in conventional modeling.

These disadvantages can be dealt with by application of non-equilibrium thermodynamics theory (NET) [13], a theory which takes into account the coupling of fluxes of heat and mass. The water flux is then not only driven by a concentration difference, it can also be driven by a thermal driving force alone. It is also possible to relax the common assumption of equilibrium at the phase-boundary water-vapor [14], using newly published transfer coefficients for water evaporation and condensation [15]. The interfaces will then be included explicitly in the modeling. A new method of discretization of the relevant equations, developed by Van der Ham et al. [16,17], provides a practical solution procedure. The method was successfully used to model water–ethanol distillation columns [18].

The aim of this work is to contribute to a more precise description of the transport of water vapor and thermal energy through the membrane in MD systems, using non-equilibrium thermodynamics. Several new experiments have been done to provide an experimental basis for the development of the model. These experiments are all done with pure water, with the same thermal driving force, and against the same pressure difference, in order to achieve a measure of the reproducibility of the processes. We will proceed to show that the theory can be used to obtain a more-detailed understanding of the observed mass flux through the membrane, in addition to the heat flux. The main process irreversibilities can be located with this knowledge. To know the location and nature of the main process inefficiencies, may give guidelines for system optimization. Such will be pointed out.

2. Coupled transport of mass and heat across a hydrophobic membrane

The theory of non-equilibrium thermodynamics (NET) provides a systematic framework for description of transport processes, including their interdependency or coupling [13,19–21]. The local entropy production is used to define the sets of conjugate fluxes and forces in this theory. We shall use the procedure of Van der Ham et al. [16,17] to integrate across the liquid-vapor interfaces of the system. Details of their derivations can be found in Appendix A. For the interfaces themselves, we shall use the procedure laid out by Kjelstrup and Bedeaux [13].

2.1. System lay-out and assumptions

Fig. 2 provides a more detailed representation of the membrane pore of the system pictured in Fig. 1. The transport in the pore is

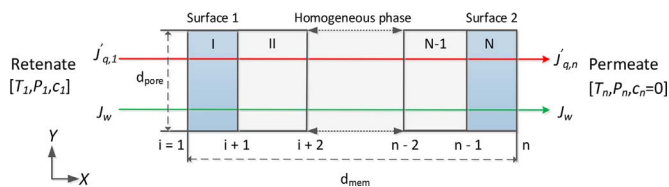


Fig. 2. Schematic representation of volume elements across a membrane pore of diameter d_{pore} . The whole rectangular box in the figure is a close-up of the pore between two black rectangles in the right-hand side of Fig. 1. The control volume to the left represents the boundary of the pore to the permeate, and the control volume to the right represents the boundary of the pore to the retentate side. The membrane is seen as a homogeneous phase of $N - 2$ control volumes. Boundaries are numbered by $i = 1, n$. Pressure, P_i , temperature, T_i , and salt chemical potential, μ_i , or concentration C_i , are known for the permeate (1) and retentate (2) sides.

considered to be one-dimensional, and we are dealing with operation under the steady state. The retentate and the permeate, on the left and right-hand sides, respectively, yield boundary conditions for the transport of mass and heat across the membrane. The pressure, P_i , temperature, T_i , and salt chemical potential, μ_i , or concentration C_i , are known for the permeate (1) and retentate (2) sides. In the experiments, to be reported here, pure water is used on both sides, and $C_i=0$. There is a transition from liquid outside the membrane to vapor in the pore, because the membrane is hydrophobic, see Ref. [22] for a good illustration of the mechanism. Some air may be trapped in the pore, without changing the chemical potential of water, or the description that follows. Heat is flowing from the retentate to the permeate side through the membrane matrix or the vapor-filled pores of the membrane. The system in Fig. 2 is considered to be isolated from the surroundings.

2.2. 1D-integrated system description

The aim is to obtain a description using measured properties, i.e. the water flux, J_w , and the flux of measurable heat at position n , $J'_{q,n}$ as variables. Subscript w refers to water and subscript q indicates that heat is transported. From the entropy production for the total system consisting of control volumes 1... N , we obtain the following force–flux relationships (see Appendix A):

$$\Delta_{\text{in}} \frac{1}{T} = r_{\text{qq}}^{\text{tot}} J'_{q,n} + r_{\text{qw}}^{\text{tot}} J_w \quad (1)$$

$$-\frac{\Delta_{\text{in}} \mu_w(T_i)}{T_i} = r_{\text{wq}}^{\text{tot}} J'_{q,n} + r_{\text{ww}}^{\text{tot}} J_w \quad (2)$$

where r_{ij}^{tot} are the total resistivities (see Eqs. (6) to (8)). The conjugate driving forces to the heat and water fluxes are $\Delta_{\text{in}} \frac{1}{T}$ and $-\frac{\Delta_{\text{in}} \mu_w(T_i)}{T_i}$, respectively. In general, the difference in the chemical driving force between points a and b at constant temperature, T_a , is equal to

$$-\frac{\Delta_{\text{ab}} \mu_{w,T}(T_a)}{T_a} = -\frac{\mu_{w,T}^b(T_a) - \mu_{w,T}^a(T_a)}{T_a} \quad (3)$$

where the symbol Δ_{ab} refers to the difference between position a and b. The chemical potential has a contribution from the vapor pressures at a and b, and from the difference in hydrostatic pressure, see e.g. [13]. The total driving force is obtained by adding the driving forces of all n connected control volumes, cf. Fig. 2. There is a total number of $n = N + 1$ control volume boundaries.

We see now from Eq. (2) how the water flux depends on the heat flux, which again depends on the thermal driving force. At zero water flux, there is a balance of forces, obtained by dividing the two equations. This will define the upper pressure one can possibly reach on the permeate side when $J_w=0$. While the resistivities on the diagonal are related to Fick's and Fourier's laws (see below), the coupling coefficients are characteristic for non-equilibrium thermodynamics. In the bulk (homogeneous) phases, they are sometimes small, and can be neglected. This will be done also here. At the interfaces, however, they are large, and must be taken along [15]. The overall coupling coefficients will therefore have nonzero contributions from the interfaces.

According to Van der Ham et al. [16,17] (see Appendix A for more details), it is possible to choose as variables the measurable heat flux, J'_q , referred to position c, and the chemical potential difference, $\Delta \mu_w$, evaluated at the temperature at position d, for a control volume between positions a and b. The equations become

$$\Delta_{\text{ab}} \frac{1}{T} = r_{\text{qq}}^{\text{ab}} J'_{q,c} + (r_{\text{qw}}^{\text{ab}} + r_{\text{qq}}^{\text{ab}} \Delta_{\text{ac}} H_{w,T}) J_w \quad (4)$$

$$-\frac{\Delta_{\text{ab}} \mu_w(T_d)}{T_d} = r_{\text{wq}}^{\text{ab}} J'_{q,c} + (r_{\text{ww}}^{\text{ab}} + r_{\text{wq}}^{\text{ab}} \Delta_{\text{ac}} H_{w,T}) J_w + \Delta_{\text{ab}} H_{w,T} \Delta_{\text{db}} \frac{1}{T} \quad (5)$$

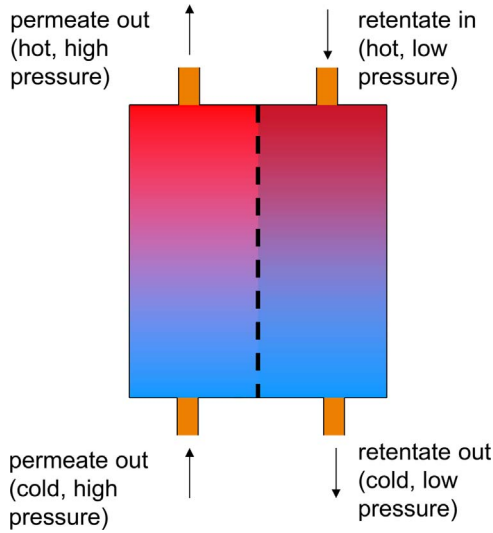


Fig. 3. Schematic representation of the experimental cell. Water is flowing from the retentate to the permeate sides through membrane pores against a fixed pressure difference of 1 bar. Temperatures are measured at the inlet and outlet on both sides. The water flux across the membrane was delivered from the retentate to the permeate, and was computed from the difference in the mass flows at steady state. A constant pressure difference was maintained across the membrane.

The coefficient r_{ij}^{ab} is the resistivity that is coupling driving force i with flux j . The resistivity r_{qq} can be related to the Fourier thermal conductivity, while the resistivity r_{ww} can be related to the diffusion coefficient for water, see Eqs. (11) and (12) below. The resistivities $r_{wq} = r_{qw}$ describe the coupling between fluxes of water and heat.

The symmetry of the problem means that the same solution must be found when boundary conditions are switched. The number of control volumes, N , in Eqs. (2) and (4) is thus an even number. We show in Appendix A how the force – flux equations are derived with four control volumes ($N=4$). The general expressions for the total resistivities that can be derived, are:

$$r_{qq}^{\text{tot}} = \sum_{k=1}^N r_{qq}^k \quad (6)$$

$$r_{qw}^{\text{tot}} = r_{wq}^{\text{tot}} = \sum_{k=1}^{N/2} r_{qw}^k + r_{qq}^k \Delta_{k,n} H_{w,T} \quad (7)$$

$$+ \sum_{k=(N/2)+1}^N r_{qw}^k + r_{qq}^k \Delta_{k+1,n} H_{w,T} r_{ww}^{\text{tot}} = \sum_{k=1}^{N/2} r_{ww}^k + (r_{qq}^k \Delta_{k,n} H_{w,T} + 2 \cdot r_{qw}^k) \Delta_{k,n} H_{w,T} \quad (8)$$

$$+ \sum_{k=(N/2)+1}^N r_{ww}^k + (r_{qq}^k \Delta_{k+1,n} H_{w,T} + 2 \cdot r_{qw}^k) \Delta_{k+1,n} H_{w,T}$$

In the expansion across the system, the enthalpy difference of water between control volume number n and k , taken at temperature T is introduced, $\Delta_{n,k} H_{w,T}$.

For the bulk part of the membrane, the contributions to Eq. (6) come from Fourier's law. The contributions to Eq. (8) come from Fick's law. In the NET formulation, these laws take the form

$$\frac{\partial T}{\partial x} = -T^2 r_{qq} J'_q \quad (9)$$

$$\frac{1}{T} \frac{\partial \mu_{w,T}}{\partial x} = -r_{ww} J_w \quad (10)$$

The membrane resistivity coefficients could then be obtained from

$$r_{qq}^{\text{mem}} = \frac{1}{\lambda_w T^2} d_{\text{mem}} \quad (11)$$

$$r_{ww}^{\text{mem}} = \frac{1}{TD_w} d_{\text{mem}} \quad (12)$$

The membrane resistance to heat transfer is given by the thermal conductivity of water vapor in the membrane pore, λ_w and the membrane thickness, d_{mem} . The resistance to mass transfer is given by the diffusion coefficient for vapor in the pore, D_w . We have assumed that the vapor is ideal. In the membrane pores, the coupling coefficients are neglected, $r_{qw}^{\text{mem}} = r_{wq}^{\text{mem}} = 0$. For the two surfaces, the full set of interface transfer coefficients provided by Wilhelmssen et al. [15] contributed to the overall resistivities. In setting up these equations, we have assumed that mass transport takes place by vapor transport only. In reality there may be air trapped inside the membrane. Stationary air will not alter the driving forces much (the vapor pressure or temperature), but it may alter the transport coefficients. This has been neglected.

3. Experimental

The proof of the MemPower principle was reported earlier [8]. The experimental set-up was a simplified version of Fig. 1, see Fig. 3. For the purpose of comparing theoretical and experimental results under the simplest possible conditions, only pure water was used on both sides of the membrane unit. Several experiments were performed. Among them, seven repeats of the same conditions were selected as a basis for the model development. The inlet and outlet temperatures of the water on the left and right hand sides were measured, along with the retentate and permeate pressures and mass flows.

The average temperature of the retentate (right hand) side was on the average always higher than the average temperature on the permeate (left hand) side. As the average temperature on each side, we took the average of the measured inlet and outlet temperatures. The pressure difference was on the average 1.2 ± 0.1 bar. Due to the temperature difference, a water flux was set up across the membrane, in spite of a pressure difference in the opposite direction, again proving the system's concept. The amount of water passing the membrane was computed from the systematic difference between the permeate and retentate streams (see below), given that the streams at the inlets were the same.

The hydrophobic membrane used in all experiments was reported earlier [8]. Such a membrane has been realized in the laboratory [22]. In this case, the membrane consisted of a selective layer and a support layer, that makes it able to withstand a pressure difference. The selective layer had pore diameters near $0.2 \mu\text{m}$ and a thickness of $5 \mu\text{m}$. Due to its hydrophobicity it was permeable to water vapor only. The support layer had pore sizes larger than $10 \mu\text{m}$ and a thickness of $80 \mu\text{m}$. It was filled with liquid water. The large pores in the support layer mean that it plays an insignificant role for the transport of heat and mass and it was therefore neglected in the simulations. The properties of the selective layer are listed in Table 1. Here, ϵ is the porosity, the void volume fraction available for vapor transport in the membrane. In view of other uncertainties the membrane is assumed to have cylindrical perpendicular pores with a tortuosity, τ , set to unity. More complex membrane structures can have a tortuosity higher than unity [23].

Table 1
Membrane properties.

Property	Symbol	Value	Unit
Membrane cross-sectional area	Ω	$6.00 \cdot 10^{-3}$	m^2
Membrane thickness	d_{mem}	$5.00 \cdot 10^{-6}$	m
Pore diameter	d_{pore}	$2.00 \cdot 10^{-7}$	m
Porosity	ϵ	0.8	–
Thermal conductivity	λ_{mem}	0.19	$\frac{\text{W}}{\text{m}\cdot\text{K}}$

Table 2

Results from seven measurements with the experimental setup reported in Section 3, showing the temperatures at inlets and outlets of the retentate and permeate flows, the pressures on the permeate side, and the mass flows on the two sides. The pressure on the retentate side, P_{ret} , is always $1.00 \cdot 10^5 \text{ N/m}^2$. The averages (see bottom row) are used in the analysis of the model, see Section 3.

$T_{\text{ret,in}}$ °C	$T_{\text{ret,out}}$ °C	$T_{\text{per,in}}$ °C	$T_{\text{per,out}}$ °C	P_{per} $10^5 \frac{\text{N}}{\text{m}^2}$	\dot{m}_{ret} $10^{-3} \frac{\text{kg}}{\text{s}}$	\dot{m}_{per} $10^{-3} \frac{\text{kg}}{\text{s}}$	J_w $10^{-2} \frac{\text{kg}}{\text{m}^2 \text{s}}$
93.09	76.83	38.36	53.96	2.0	3.42	3.49	1.52
94.10	77.27	38.14	54.30	2.2	3.31	3.38	1.50
94.05	77.12	38.01	53.97	2.2	3.28	3.35	1.48
94.05	76.87	37.91	53.85	2.3	3.25	3.33	1.46
94.02	76.79	37.90	53.70	2.3	3.17	3.24	1.41
94.07	77.31	38.43	54.42	2.3	3.36	3.44	1.47
94.09	77.29	37.75	53.70	2.3	3.39	3.46	1.41
94.1	77.0	38.1	54.0	2.2	3.31	3.38	1.47
± 0.1	± 0.2	± 0.2	± 0.3	± 0.1	± 0.09	± 0.07	± 0.05

Table 3

Average measured temperatures, pressures and water flux, computed from Table 2. Uncertainties are within 0.1 °C, 0.1 bar and $2 \cdot 10^{-3} \text{ kg}/(\text{m}^2 \text{ s})$.

	$T_{\text{ret,avg}}$ °C	$T_{\text{per,avg}}$ °C	P_{ret} $10^5 \frac{\text{N}}{\text{m}^2}$	P_{per} $10^5 \frac{\text{N}}{\text{m}^2}$	J_w $10^{-2} \frac{\text{kg}}{\text{m}^2 \text{s}}$
Average	85.5	46.0	1.0	2.2	1.5

3.1. Data reduction

The results from all seven experiments are presented in Table 2. The average quantities relevant for the development of the model are extracted to Table 3. The mass flow observed through the membrane gives the membrane water flux J_{mem} from

$$J_{\text{mem}} = \dot{m}_{\text{mem}}/\Omega \quad (13)$$

where \dot{m}_{mem} is the mass flow across the membrane and Ω is the cross-sectional area of the MemPower system. The water flux can also be referred to the area accessible to vapor transport, via the membrane porosity, ε . The relation between this water flux, J_w , and J_{mem} , for cylindrical pores is

$$J_w = J_{\text{mem}}/\varepsilon \quad (14)$$

4. Numerical data input and solution procedures

All simulations refer to Fig. 2 and use the membrane properties presented in Table 1 and below. The boundary conditions of the retentate and permeate sides, as given in Table 3 could then be used to compute the mass and heat fluxes through the membrane.

4.1. Numerical data input

Thermodynamic properties of water were calculated using the IF97 model in FluidProp [24]. The inputs to this model are the temperature and pressure of the control volume in question. Surface resistivities for water were taken from Wilhelmson et al. [15], assuming that the surface is flat.

For the membrane thermal conductivity, we used the vapor value, $\lambda_{\text{vap}} = 2.30 \cdot 10^{-2} \text{ W}/(\text{mK})$, and the polymer matrix value from Table 1. The partial derivative $\partial\mu_{w,T}/\partial c_w$ was taken to be unity (ideal vapor). The value of D_w was modeled with the Knudsen diffusion model, following [22,9,10], as the pore diameter was always smaller than the mean free path (calculated from the kinetic theory-formula to $2.6 \cdot 10^{-7} \text{ m}$).

$$D_w = \frac{d_{\text{pore}}}{3} \sqrt{\frac{8RT}{\pi M_w}} = 4.27 \cdot 10^{-5} \frac{\text{m}}{\text{s}^2} \quad (15)$$

The result did not vary much with temperature around this average value.

4.2. Solution procedure. NET

The equations that constitute the NET model were presented in Section 2. An overview of the solution procedure for the one-dimensional problem is given in Fig. 4. The procedure which follows [16], starts by defining the retentate and permeate boundary temperature and pressure, using Table 3, and computing the corresponding overall driving forces X_j^{tot} Eqs. (1) and (2). In the next step (2), the number of membrane control volumes is chosen, N . There are now $n = N + 1$ control volume boundaries. The initial temperature and pressure profiles, and the molar enthalpies at the control volume boundaries can then be obtained. From this information, the resistivities r_{ij}^{CV} of all control volumes for the membrane and for the surface are computed (step 3). With the molar enthalpies, $H_{j,T}$, at all control volume boundaries, and the initial temperature and pressure profiles, the total resistivities r_{ij}^{tot} are next computed (step 4) using r_{ij}^{CV} .

From the overall driving forces, X_j^{tot} , and r_{ij}^{tot} , one can next compute the water flux J_j and the measurable heat flux at boundary n , $J'_{q,n}$ (step 5). The measurable heat flux profile, $J'_{q,i}$, follows (step 6) using the energy balances $J'_{q,i} = J'_{q,n} + \Delta_{i,n} H_w J_w$.

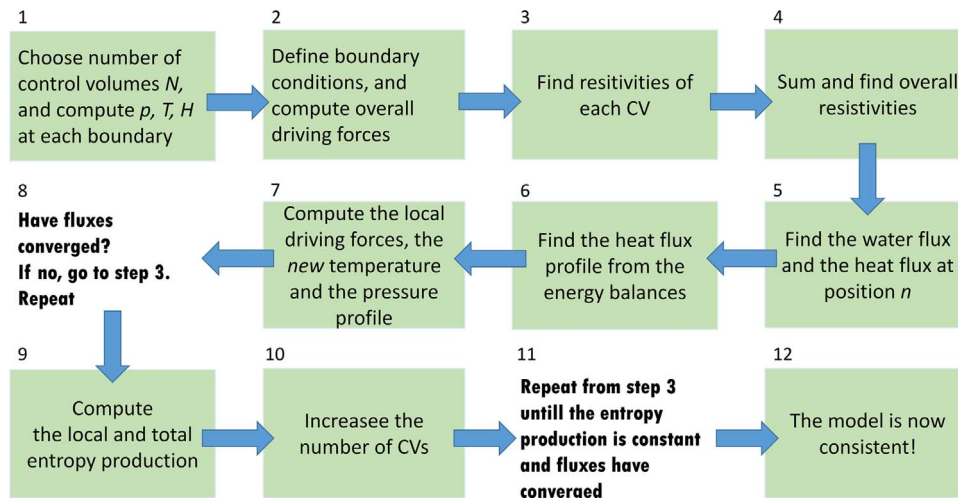


Fig. 4. Flow sheet illustrating how the NET model is solved. For more details, see text.

With this information the local driving forces of the control volumes, ΔX_j^{CV} , are available (step 7) using r_{ij}^{CV} , J_j and J'_q . A new temperature profile $T(x)$ and a new pressure profile $p(x)$ is next available.

Steps 3–7 are repeated until the fluxes have converged, and the total entropy production can be computed using X_j^{CV} , J'_q and J_j , as well as the entropy balance (step 8). The number of membrane control volumes can then be raised (step 9). Steps 3–9 are repeated until the entropy production is constant and the fluxes have converged. The solution will then obey consistency checks as described in Appendix B.

The resistivities of the control volumes (step 3 in the figure) were calculated for the local temperature and pressure. Membrane resistivities were multiplied with the thickness of the control volume in the x-direction, $d_{CV} = d_{mem}/N$. The surface resistivities already include the surface thickness. The total resistivities, r_{ij}^{tot} , were calculated using equations in Section 2.2. The fluxes J_j and $J'_{q,n}$ were obtained by dividing the overall driving force vector X_j^{tot} by the total resistivity matrix composed of r_{ij}^{tot} .

The side with the highest temperature (T_n , see Fig. 2) was used as the reference temperature for enthalpy calculations. This was done in order to make sure that the enthalpies inside the membrane always apply to water in the vapor phase. The enthalpies used in the calculation of the heat flux through the membrane were first taken at constant temperature. The energy balance over the membrane is then not obeyed. The measurable heat flux at the retentate side, $J'_{q,1}$, was in the end recalculated for the control volume boundaries to conform with the energy balance;

$$J'_{q,i} = J'_{q,i+1} + J_w \Delta_{i,1} H_w \quad (16)$$

The total energy flux through the membrane pore:

$$J_q = J'_{q,i} + J_w H_i \quad (17)$$

is constant in the calculations.

When heat conduction in the membrane is considered, the measurable heat flux through the membrane cross-sectional area is calculated as:

$$J_{q,mem,i} = \epsilon J'_{q,i} + (1 - \epsilon) \lambda_{mem} \frac{dT}{d_{mem}} \quad (18)$$

where λ_{mem} is taken from Table 1. Otherwise, $\lambda_{mem} = 0$.

Two iteration loops were included in the calculations, for which the following convergence criterion was used: $(|1 - J(i+1)/J(i)| < 0.0001)$. Five iteration steps were normally needed to obtain the final pressure, temperature profile and entropy production, with 10 membrane control volumes, and two surface control volumes. The solution procedure was tested for inversion of the boundary conditions. An inversion did not change the outcome of the calculations, as required. In order to ensure that the model was thermodynamically consistent, several additional validation tests were performed. They are explained in detail in Appendix B, and reported as Results.

4.3. Solution procedure. Conventional model

The conventional model of membrane distillation described the transport of water by Fick's law after introduction of vapor pressures via the ideal gas law $RTdc_w = dP_w^*$ [9,10].

$$J_{mem} = \epsilon J_w = -\epsilon B \frac{\Delta p_w^*}{d_{mem}} \quad (19)$$

where the driving force is the gradient in the saturation pressure of water vapor. The water is affected by the temperature gradient only indirectly in this description, via the temperature dependence of p_w^* along the x-axis [25,12]. The flux refers to the accessible area, the cross-sectional area of the pores. The membrane permeability $B = \frac{D_w}{RT}$, where D_w is the diffusion coefficient as before.

The heat flux through the membrane has contributions from

transport of latent heat and from conduction. Conduction takes place across the membrane matrix as well as the pores. The combined contributions lead to [26,27,11,3]

$$J_q^{per} = J_{mem} \Delta H_{vap,w} - \lambda \frac{\Delta T}{d_{mem}} \quad (20)$$

Where J_q^{per} is the total measurable heat flux, λ the thermal conductivity of the membrane; pores and polymer network combined, ΔT is the temperature difference across the membrane, and $\Delta H_{vap,w}$ the enthalpy of evaporation of water at the entrance to the pores. The effective thermal conductivity is given by

$$\lambda = \epsilon \lambda_{vap} + (1 - \epsilon) \lambda_{mem} \quad (21)$$

A one-dimensional system was constructed to compute results. Only one control volume was used for the membrane pore, $N=1$ in Fig. 2. There are no surface control volumes in this model. The Eqs. (19) and (20) were solved in the following stepwise manner. The boundary conditions were defined for the retentate and permeate, similar to step 1 in the NET model. The overall driving forces were calculated, using the temperatures and vapor pressures at the membrane boundaries. With knowledge of thermophysical properties, D_w , λ and $\Delta H_{vap,w}$, the mass flux J_{Lw} becomes available. The heat flux, J_q^{per} , is finally calculated from Eq. (20).

5. Results and discussion

The experimental results are reported in Table 2, cf. Section 3 for data analysis. The temperatures and pressures from this table were used as boundary conditions in the simulation (see Table 3). Simulation results are reported and discussed in the sections that follow this one. A first aim is to compute the water flux across the membrane and compare to the experimental water flux across the membrane (last column of Table 2).

The average water flux, J_{Lw} , was computed from Eq. (14) and the observed systematic difference between the permeate and the retentate mass flows (resulting in \dot{m}_{mem}), and related to the difference in the average of the inlet and outlet temperatures in Table 2. The results are given in Table 3. The temperatures and pressures in this table are used as boundary conditions for the calculations reported in the next section. The water flux of Table 3 will be compared to the simulated one (see next section).

5.1. NET simulation results

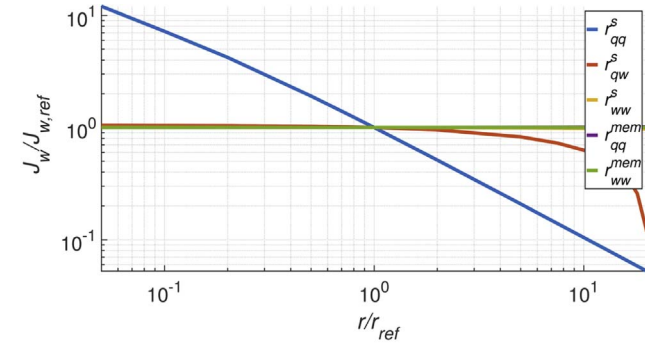
Table 4 (top row) presents results of the NET model simulations for the given boundary conditions given from the experiments. The model was described in Section 4.2.

The simulated mass flux, $1.1 \cdot 10^{-3}$ kg/(m²s), is smaller than the experimental mass flux, $1.5 \cdot 10^{-2}$ kg/(m²s) by one order of magnitude. The experimental value has a large uncertainty, however. It appears as a difference between two large numbers, but obtains reliability because the permeate side value is systematically larger than the retentate value in all seven experiments. A lower limit for J_{Lw} can be obtained from the uncertainty of the experimental flux; $2 \cdot 10^{-3}$ kg/(m²s). This is close to the experimental value. Lee et al. [22] report an experimental value for the

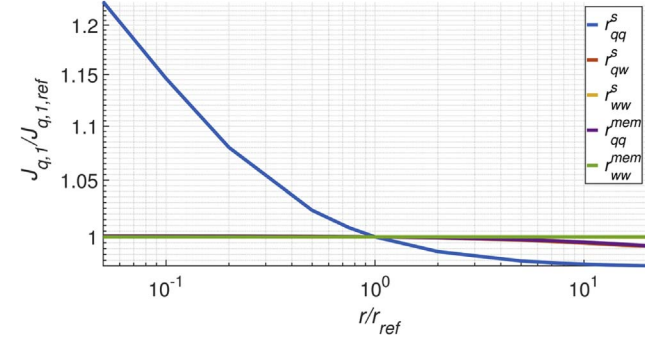
Table 4

Simulation results for the 1D-NET model. The membrane conductivity is finite (top row) or zero (middle row). The surface resistivities also set to a negligible value (bottom row).

	J_{Lw} kg m ² s	$J_{q,ret}'$ J m ² s	$J_{q,per}'$ J m ² s	$J_{q,mem}'$ J m ² s
Finite λ_{mem}	$1.1 \cdot 10^{-3}$	$3.1 \cdot 10^5$	$3.1 \cdot 10^5$	$3.0 \cdot 10^5$
$\lambda_{mem} = 0$	$1.1 \cdot 10^{-3}$	$8.0 \cdot 10^3$	$8.2 \cdot 10^3$	0
No surface effect	1.4	$4.1 \cdot 10^5$	$4.4 \cdot 10^5$	0



(a) The mass flux as a function of the scaled resistivities.



(b) The heat flux as a function of the scaled resistivities.

Fig. 5. The dependence of the fluxes on the overall Onsager resistivities.

mass flux in osmotic experiments with a hydrophobic membrane, against a small pressure difference, of the same order of magnitude as we obtain. This gives support to the lower estimates.

The simulated value is rather sensitive to the surface resistivities (see below). We have used surface transfer coefficients for pure water. With pore diameters in the nanometer range, the presence of the hydrophobic membrane material may enhance the water transport through the phase boundary. It is known that a concave shape of the liquid-vapor interface will reduce the resistivities [15]. This will make a better fit to the experimental value. Given the uncertainties, however, we prefer to not attempt to tailor the model to experimental results, but continue with observing trends. The meaning is to obtain knowledge that can lead to further research.

A sensitivity analysis was therefore carried out for the resistivities, to see their impact. The results are shown in Fig. 5. The resistivities were varied one by one, and their influence on the water flux and on the measurable heat flux was computed. The x -axis shows the new resistivity divided by the reference; which is the resistivity according to Wilhelmsen et al., $r_{ij}/r_{ij,ref}$. The y -axis show the impact on the two fluxes. The thermal resistivity of the surface, r_{qq}^s , has the most important influence on the mass flux and heat flux. Also r_{qw}^s is significant. The mass flux can increase or decrease by an order of magnitude, should the resistivity decrease or increase. This is important, and should be tested experimentally. In this context, it is interesting that the mass flux observed by Lee et al. [22] for small osmotic pressure differences across hydrophobic pores, is order of magnitude the same as our experimental values. This gives support to our effort to take surface coefficients into account. Surface resistivities are therefore central for accurate information on the mass flux. The coefficients are less important for the heat flux, however. A change in the heat flux is within 20% for similar variations in the coefficients. The results show that the membrane resistivities have a negligible impact on both fluxes. This could mean that our assumption of a negligible coupling coefficient in the membrane is good.

The heat flux on the permeate and retentate sides in Table 4 differ

from the heat flux in the membrane, due to the latent heat carried by the mass flux, but this is a small contribution. The heat flux is largely affected by the thermal conductivity of the membrane polymer. When the membrane conductivity is equal to zero ($\lambda_{mem} = 0$, center row results), the heat flux drops more than one order of magnitude. For the heat flux, we have no measurements to compare to. If also this is measured, there would be a second useful handle for model development. A membrane that is less conductive to heat is an advantage for the mass flux, see Fig. 5a.

5.2. Properties of the NET model

The model constructed with NET was subject to several validation tests, see Appendix B. All were confirmed, as described below. This does not only give credibility to the model. It provides also a solid base for further development.

Total and local entropy production. In order to test for agreement with the second law of thermodynamics, we computed the total entropy production of the system in two ways, from the entropy balance over the total system, $\sigma_{balance}^{tot}$, and from the global fluxes and forces, σ_{JX}^{tot} . Agreement was obtained within less than 0.1%, $\sigma_{balance}^{tot} = \sigma_{JX}^{tot} = 3.53 \text{ J/m}^2\text{Ks}$.

The local entropy production, σ_T , was also calculated. The σ_T (not shown) was positive in all control volumes, as it should be. Almost all entropy production took place at the membrane boundaries, the permeate side more than the retentate side, see Table 9 for more details. This reflects again the importance of the surface resistivities. Most of the dissipation of energy takes place here (86%). This finding is supported by the findings of Lee et al. [22], that the surface played a central role for the rate of water transfer.

Overall and local driving forces. The overall thermal driving force is shown in Table 5. The overall thermal driving force and the sum of the local thermal driving forces are equal. The overall chemical driving force, evaluated at T_1 , is shown in Table 6. Again, the overall driving force is equal to the sum of the local chemical driving forces; meaning that the model is thermodynamically correct.

Resistivity coefficients. It was next verified that the local, as well as the total resistivity matrices obey Onsager symmetry [13]. Coefficients in the total resistivity matrix are shown in Table 7. The main coefficients are positive as they should be. The coupling coefficients are in this case negative, meaning that heat is transported in the same direction as mass. Because the coupling coefficient in the membrane is set to zero; the contribution from the surfaces dominate completely the value of the coupling coefficients.

5.3. Transport properties. Numerical results

Table 8 provides detailed insight into the coefficients that con-

Table 5

The overall thermal driving force (in $1/\text{K}$), calculated from the overall boundary conditions, from the sum of local driving forces and from the force-flux relations.

$\Delta \ln \frac{1}{T}$	$\sum_{k=1}^{n-1} \Delta_{ab}^k \frac{1}{T}$	$r_{qq}^{tot} J_{q,n} + r_{qw}^{tot} J_w$
$3.45 \cdot 10^{-4}$	$3.45 \cdot 10^{-4}$	$3.45 \cdot 10^{-4}$

Table 6

The chemical driving force (in $\text{J}/(\text{K mol})$), calculated from the overall boundary conditions, from the sum of local driving forces and from the force-flux relations.

$-\frac{\Delta \ln \mu_w(T)}{T_1}$	$\sum_{k=1}^{n-1} -\frac{\Delta_{ab}^k \mu_w(T)}{T_1}$	$J_{wq}^{tot} J_{q,n} + J_{ww}^{tot} J_w$
$-6.3 \cdot 10^{-3}$	$-6.3 \cdot 10^{-3}$	$-6.3 \cdot 10^{-3}$

Table 7

Overall resistivities for mass and heat transport in the hydrophobic membrane of MemPower.

r_{qq}^{tot} $\frac{\text{m}^2 \text{ s}}{\text{J-K}}$	r_{qw}^{tot} $\frac{\text{m}^2 \text{ s}}{\text{mol-K}}$	r_{wq}^{tot} $\frac{\text{m}^2 \text{ s}}{\text{mol-K}}$	r_{ww}^{tot} $\frac{\text{J-m}^2 \text{ s}}{\text{mol-K}}$
$4.95 \cdot 10^{-8}$	$-2.08 \cdot 10^{-3}$	$-2.08 \cdot 10^{-3}$	$2.75 \cdot 10^2$

tribute to the overall coefficients of Table 7. Results for four control volumes are shown. The surface resistivities at the permeate side are somewhat higher than on the retentate side surface, explaining the higher entropy production on this side. This is due to the lower temperature on the permeate side of the system. The resistivities of the membrane near the two surfaces, increase slightly, going from the retentate side to the permeate side. The surface resistance is about two orders of magnitude larger than the membrane resistance. The negative coupling coefficient of the surface means that uphill transport of water can take place.

5.3.1. Contributions to the entropy production

The contributions to the global entropy production are shown in % in Table 9. The thermal contribution dominates completely, and that the dominating part is at the permeate side. The contribution from the chemical driving force is small, but not zero. The surface facing the permeate side is clearly a target for material optimization and further studies. By lowering the surface resistivity to heat transport, the dominating thermal term can be much reduced. An increase in the pressure difference across the membrane did not markedly affect the results.

5.4. Results from the conventional model

The results from the conventional model, using input from Table 3 are presented in Table 10. The fluxes were calculated as described in Section 4.3. A scenario with an insulating membrane, $\lambda_{\text{mem}} = 0$, is also presented in this Table 10. We see that the measured mass flux is now over-predicted by 3 orders of magnitude. This can be somewhat mended by including a tortuosity factor, which is usual higher than unity due to a more complex membrane structure; by reducing the

Table 8

Average resistivities of the retentate surface CV, the CV next to this surface (1), the CV next to surface (2) and permeate surface CV.

Control volume (CV)	r_{qq} $\frac{\text{m}^2 \text{ s}}{\text{J-K}}$	r_{qw} $\frac{\text{m}^2 \text{ s}}{\text{mol-K}}$	r_{ww} $\frac{\text{J-m}^2 \text{ s}}{\text{mol-K}}$
Retentate surface CV	$5.50 \cdot 10^{-9}$	$-2.15 \cdot 10^{-4}$	27.44
CV next to retentate surface	$1.74 \cdot 10^{-10}$	0	$3.31 \cdot 10^{-5}$
CV next to permeate surface	$1.76 \cdot 10^{-10}$	0	$3.33 \cdot 10^{-5}$
Permeate surface CV	$4.23 \cdot 10^{-8}$	$-1.80 \cdot 10^{-3}$	$2.44 \cdot 10^2$

Table 9

Contributions in percent to the overall entropy production from the surfaces and the membrane.

σ_{T_i}	$J_q' \Delta \frac{1}{T} (\%)$	$J_w \frac{\Delta \mu_w(T)}{T} (\%)$	$\sigma_{T_i}^{\text{tot}} (\%)$
$\sigma_{T_i}^{s,1}$	12	0	12
$\sigma_{T_i}^h$	2	0	2
$\sigma_{T_i}^{s,2}$	85	1	86
$\sigma_{T_i}^{\text{tot}}$	99	1	100

Table 10

Results for the conventional 1D model. The membrane thermal conductivity is finite (top row) or zero (bottom row).

J_w $\frac{\text{kg}}{\text{m}^2 \text{ s}}$	$J_{q,\text{ret}}'$ $\frac{\text{J}}{\text{m}^2 \text{ s}}$	$J_{q,\text{per}}'$ $\frac{\text{J}}{\text{m}^2 \text{ s}}$	$J_{q,\text{mem}}'$ $\frac{\text{J}}{\text{m}^2 \text{ s}}$
2.12	$5.40 \cdot 10^6$	$5.40 \cdot 10^6$	$3.00 \cdot 10^5$
2.12	$5.10 \cdot 10^6$	$5.10 \cdot 10^6$	0

vapor diffusion coefficient (due to presence of air in the voids), or by including larger membrane resistances. This may reduce the mass flux, maybe as much as an order of magnitude. It is difficult to see how the overall resistivities could be much larger, without including a surface resistance. This suspicion was confirmed when we replaced the present surface resistivities with values that were similar to bulk values. By neglecting the special properties of the surface, we recovered in our model the large water flux of the conventional model, see bottom row of Table 4.

Also the support layer may play a role in reducing the temperature difference across the membrane, thereby reducing the driving force. Such a reduction will increase the gap between the NET model and the conventional model, however.

The two ways to describe the system, produces water fluxes which differ by orders of magnitude. Taking the experimental result as a reference, the conventional model largely over-predicts this flux, while it is somewhat under-predicted by NET.

The conventional model oversimplifies the description, and is not able to describe the entropy production. The NET model has been checked for consistency and gives further insight into where energy is dissipated (at the membrane surfaces, in particular on the permeate side), and can provide a basis for further work through that. Efforts should be made to improve conditions in particular for heat transport on this side. From the sensitivity of the results to the choice of resistivities, demonstrated above, a meaningful step forward seems to be the determination of membrane surface resistivities. How does the membrane surface limit the transport, and how precisely does the hydrophobic nature of the membrane affects the resistivities? The precise location and value of the driving forces at this location is clearly important for the efficiency of the unit.

6. Conclusion

We have used non-equilibrium thermodynamics to describe membrane distillation of water against a pressure difference, as in the MemPower concept, assuming that the transport takes place in 1 dimension. The theory can be used to predict a water flux directly driven by a thermal driving force, unlike in most other models, where the temperature-dependent vapor pressure drives the flux. Using recently published transport coefficients for pure water at a flat surface, and driving forces of the experiment, we compute the water flux, and argue that it is reasonable compared to the experimental result. By taking into account the hydrophobic nature of the membrane, better agreement seems within reach. The conventional model, on the other hand, over-predicts the mass flux largely. Better knowledge of surface

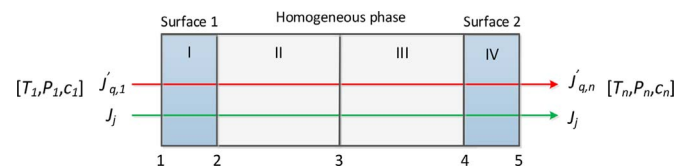


Fig. A.6. A model of the symmetrical system consisting of 4 control volumes. Boundary conditions are given in terms of pressure and temperature, p_i, T_i , at position $i=1$ and 5 . We are interested in the water flux, J_w , and the varying measurable heat flux across the system.

transfer coefficient for pores in hydrophobic membranes may help improve the MemPower concept. Modeling of more realistic operating conditions is an interesting next step.

Acknowledgment

This work was sponsored by NWO Exacte Wetenschappen (Physical Sciences) for the use of supercomputer facilities, with financial support

from the Nederlandse Organisatie voor Wetenschappelijk Onderzoek (Netherlands Organisation for Scientific Research, NWO). TJHV acknowledges NWO-CW (Chemical Sciences) for a VICI grant. SK is grateful to TU Delft for an adjunct professorship until 2015. This technology is developed by Nederlands Organisation for Applied Scientific Research (TNO). There is no conflict of interests between the parties.

Appendix A. Local and global forces and conjugate fluxes

Consider for the sake of illustration that the system consists of four control volumes, a volume including the surface (I), two volumes in the homogeneous membrane (II and III) and a volume containing the other surface (IV). The symmetrical arrangement is shown in Fig. A.6.

Following Kjelstrup and Bedeaux [13] the force–flux relations for each control volume are:

$$\Delta_{ab} \frac{1}{T} = r_{qq}^{ab} J'_{q,a} + r_{qw}^{ab} J_w \quad (\text{A.1})$$

$$-\frac{\Delta_{ab} \mu_w(T_b)}{T_b} = r_{wq}^{ab} J'_{q,a} + r_{ww}^{ab} J_w \quad (\text{A.2})$$

where a and b are the boundaries of the control volume. The measurable heat flux J'_q refers to point a, while the chemical potential difference refer to point b, see Kjelstrup and Bedeaux [13] for more details. For the four control volumes in Fig. A.6, we obtain:

Control volume I

$$\Delta_{12} \frac{1}{T} = r_{qq}^I J'_{q,1} + r_{qw}^I J_w \quad (\text{A.3})$$

$$-\frac{\Delta_{12} \mu_w(T_2)}{T_2} = r_{wq}^I J'_{q,1} + r_{ww}^I J_w \quad (\text{A.4})$$

Control volume II

$$\Delta_{23} \frac{1}{T} = r_{qq}^{II} J'_{q,2} + r_{qw}^{II} J_w \quad (\text{A.5})$$

$$-\frac{\Delta_{23} \mu_w(T_3)}{T_3} = r_{wq}^{II} J'_{q,2} + r_{ww}^{II} J_w \quad (\text{A.6})$$

Control volume III

$$\Delta_{34} \frac{1}{T} = r_{qq}^{III} J'_{q,4} + r_{qw}^{III} J_w \quad (\text{A.7})$$

$$-\frac{\Delta_{34} \mu_w(T_3)}{T_3} = r_{wq}^{III} J'_{q,4} + r_{ww}^{III} J_w \quad (\text{A.8})$$

Control volume IV

$$\Delta_{45} \frac{1}{T} = r_{qq}^{IV} J'_{q,5} + r_{qw}^{IV} J_w \quad (\text{A.9})$$

$$-\frac{\Delta_{45} \mu_w(T_4)}{T_4} = r_{wq}^{IV} J'_{q,5} + r_{ww}^{IV} J_w \quad (\text{A.10})$$

A.1. From the local to the overall description

Boundary conditions are only known at position 1 and 5 (=c). In order to make use of these, we introduce as variables, the measurable heat flux at position 5 and the chemical potential difference at temperature T_1 . The heat flux at any position is related to that of position 5 via the energy balance:

$$J'_{q,c} = J'_{q,a} + \Delta_{ca} H_{w,T} J_w \quad (\text{A.11})$$

$$-\frac{\Delta_{ab} \mu_w(T_d)}{T_d} = -\frac{\Delta_{ab} \mu_w(T_b)}{T_b} - \Delta_{ab} H_{w,T} \Delta_{bd} \frac{1}{T} \quad (\text{A.12})$$

The chemical potential differences in the last line were related by the van't Hoff equation, see [17] for more details. Applying these equations, we rewrite all measurable heat fluxes in Eqs. (A.3) to (A.10) to contain $J'_{q,5}$ and all chemical potential differences to refer to T_1 . This yields:

Control volume I

$$\Delta_{12} \frac{1}{T} = r_{qq}^I J'_{q,5} + (r_{qw}^I + r_{qq}^I \Delta_{15} H_{w,T}) J_w \quad (\text{A.13})$$

$$-\frac{\Delta_{12}\mu_w(T_1)}{T_1} = r_{wq}^I J'_{q,5} + (r_{ww}^I + r_{wq}^I \Delta_{15} H_{w,T}) J_w + \Delta_{12} H_{w,T} \Delta_{12} \frac{1}{T} \quad (\text{A.14})$$

Control volume II

$$\Delta_{23} \frac{1}{T} = r_{qq}^{II} J'_{q,5} + (r_{qw}^{II} + r_{qq}^{II} \Delta_{25} H_{w,T}) J_w \quad (\text{A.15})$$

$$-\frac{\Delta_{23}\mu_w(T_1)}{T_1} = r_{wq}^{II} J'_{q,5} + (r_{ww}^{II} + r_{wq}^{II} \Delta_{25} H_{w,T}) J_w + \Delta_{23} H_{w,T} \Delta_{13} \frac{1}{T} \quad (\text{A.16})$$

Control volume III

$$\Delta_{34} \frac{1}{T} = r_{qq}^{III} J'_{q,5} + (r_{qw}^{III} + r_{qq}^{III} \Delta_{45} H_{w,T}) J_w \quad (\text{A.17})$$

$$-\frac{\Delta_{34}\mu_w(T_1)}{T_1} = r_{wq}^{III} J'_{q,5} + (r_{ww}^{III} + r_{wq}^{III} \Delta_{45} H_{w,T}) J_w + \Delta_{34} H_{w,T} \Delta_{13} \frac{1}{T} \quad (\text{A.18})$$

Control volume IV

$$\Delta_{45} \frac{1}{T} = r_{qq}^{IV} J'_{q,5} + (r_{qw}^{IV} + r_{qq}^{IV} \Delta_{55} H_{w,T}) J_w \quad (\text{A.19})$$

$$-\frac{\Delta_{45}\mu_w(T_1)}{T_1} = r_{wq}^{IV} J'_{q,5} + (r_{tot}^{IV} + r_{wq}^{IV} \Delta_{55} H_{w,T}) J_w + \Delta_{45} H_{w,T} \Delta_{14} \frac{1}{T} \quad (\text{A.20})$$

We see that the differences in the inverse temperatures on the right-hand sides of Eqs. (A.14), (A.16), (A.18) and (A.20) are given by (sums of) Eqs. (A.13), (A.15) and (A.17). We execute these summations and substitutions, and obtain:

$$\Delta_{13} \frac{1}{T} = (r_{qq}^I + r_{qq}^{II}) J'_{q,5} \quad (\text{A.21})$$

$$+(r_{qw}^I + r_{qq}^I \Delta_{15} H_{w,T} + r_{qw}^{II} + r_{qq}^{II} \Delta_{25} H_{w,T}) J_w \Delta_{14} \frac{1}{T} = (r_{qq}^I + r_{qq}^{II} + r_{qq}^{III}) J'_{q,5} \quad (\text{A.22})$$

$$+(r_{qw}^I + r_{qq}^I \Delta_{15} H_{w,T} + r_{qw}^{II} + r_{qq}^{II} \Delta_{25} H_{w,T} + r_{qw}^{III} + r_{qq}^{III} \Delta_{45} H_{w,T}) J_w - \frac{\Delta_{12}\mu_w(T_1)}{T_1} = (r_{wq}^I + r_{qq}^I \Delta_{12} H_{w,T}) J'_{q,5} \quad (\text{A.23})$$

$$+(r_{tot}^I + r_{wq}^I \Delta_{15} H_{w,T} + (r_{qw}^I + r_{qq}^I \Delta_{15} H_{w,T}) \Delta_{12} H_{w,T}) J_w - \frac{\Delta_{23}\mu_w(T_1)}{T_1} = (r_{wq}^{II} + (r_{qq}^I + r_{qq}^{II}) \Delta_{23} H_{w,T}) J'_{q,5} \quad (\text{A.24})$$

$$+(r_{tot}^{II} + r_{wq}^{II} \Delta_{25} H_{w,T} + (r_{qw}^I + r_{qq}^I \Delta_{15} H_{w,T} + r_{qw}^{II} + r_{qq}^{II} \Delta_{25} H_{w,T}) \Delta_{23} H_{w,T}) J_w - \frac{\Delta_{34}\mu_w(T_1)}{T_1} = (r_{wq}^{III} + (r_{qq}^I + r_{qq}^{II}) \Delta_{34} H_{w,T}) J'_{q,5} \quad (\text{A.25})$$

$$+(r_{tot}^{III} + r_{wq}^{III} \Delta_{45} H_{w,T} + (r_{qw}^I + r_{qq}^I \Delta_{15} H_{w,T} + r_{qw}^{II} + r_{qq}^{II} \Delta_{25} H_{w,T}) \Delta_{34} H_{w,T}) J_w - \frac{\Delta_{45}\mu_w(T_1)}{T_1} = (r_{wq}^{IV} + (r_{qq}^I + r_{qq}^{II} + r_{qq}^{III}) \Delta_{45} H_{w,T}) J'_{q,5} \quad (\text{A.26})$$

$$+(r_{tot}^{IV} + r_{wq}^{IV} \Delta_{55} H_{w,T} + (r_{qw}^I + r_{qq}^I \Delta_{15} H_{w,T} + r_{qw}^{II} + r_{qq}^{II} \Delta_{25} H_{w,T} + r_{qw}^{III} + r_{qq}^{III} \Delta_{45} H_{w,T}) \Delta_{45} H_{w,T}) J_w$$

We are now in a position to sum forces across the system, keeping in mind that $r_{qw} = r_{wq}$ and $\Delta_{55} H_{w,T} = 0$. The expressions for the total resistivities r_{ij}^{tot} are:

$$r_{qq}^{\text{tot}} = r_{qq}^I + r_{qq}^{II} + r_{qq}^{III} + r_{qq}^{IV} \quad (\text{A.27})$$

$$r_{qw}^{\text{tot}} = r_{qw}^I + r_{qq}^I \Delta_{15} H_{w,T} + r_{qw}^{II} + r_{qq}^{II} \Delta_{25} H_{w,T} \quad (\text{A.28})$$

$$+ r_{qw}^{III} + r_{qq}^{III} \Delta_{45} H_{w,T} + r_{qw}^{IV} + r_{qq}^{IV} \Delta_{55} H_{w,T} r_{wq}^{\text{tot}} = r_{wq}^I + r_{qq}^I \Delta_{12} H_{w,T} + r_{wq}^{II} + (r_{qq}^I + r_{qq}^{II}) \Delta_{23} H_{w,T} \quad (\text{A.29})$$

$$+ r_{wq}^{III} + (r_{qq}^I + r_{qq}^{II}) \Delta_{34} H_{w,T} + r_{wq}^{IV} + (r_{qq}^I + r_{qq}^{II} + r_{qq}^{III}) \Delta_{45} H_{w,T} = r_{qw}^{\text{tot}} r_{ww}^{\text{tot}} = r_{tot}^I + r_{wq}^I \Delta_{15} H_{w,T} + (r_{qw}^I + r_{qq}^I \Delta_{15} H_{w,T}) \Delta_{12} H_{w,T} \quad (\text{A.30})$$

$$+ r_{ww}^{II} + r_{wq}^{II} \Delta_{25} H_{w,T} + (r_{qw}^I + r_{qq}^I \Delta_{15} H_{w,T} + r_{qw}^{II} + r_{qq}^{II} \Delta_{25} H_{w,T}) \Delta_{23} H_{w,T} + r_{ww}^{III} + r_{wq}^{III} \Delta_{45} H_{w,T} + (r_{qw}^I + r_{qq}^I \Delta_{15} H_{w,T} + r_{qw}^{II} + r_{qq}^{II} \Delta_{25} H_{w,T}) \Delta_{34} H_{w,T} + r_{ww}^{IV}$$

$$+ r_{wq}^{IV} \Delta_{55} H_{w,T} + (r_{qw}^I + r_{qq}^I \Delta_{15} H_{w,T} + r_{qw}^{II} + r_{qq}^{II} \Delta_{25} H_{w,T} + r_{qw}^{III} + r_{qq}^{III} \Delta_{45} H_{w,T}) \Delta_{45} H_{w,T} = r_{ww}^I + r_{ww}^{II} + r_{ww}^{III} + r_{ww}^{IV} \\ + 2 \cdot (r_{wq}^I \Delta_{15} H_{w,T} + r_{wq}^{II} \Delta_{25} H_{w,T} + r_{wq}^{III} \Delta_{45} H_{w,T} + r_{wq}^{IV} \Delta_{55} H_{w,T}) + r_{qq}^I (\Delta_{15} H_{w,T})^2 + r_{qq}^{II} (\Delta_{25} H_{w,T})^2 \\ + r_{qq}^{III} (\Delta_{45} H_{w,T})^2 + r_{qq}^{IV} (\Delta_{55} H_{w,T})^2$$

These equations enable us to construct the global resistivities to transport of mass and heat, from knowledge of local properties. We observe that the Onsager relations apply also to the global description.

Appendix B. Thermodynamic consistency

Several computations can be done to check the model for thermodynamic consistency. It follows a detailed description of the conditions reported in the paper.

1. The entropy balance and the entropy production. The entropy production, as calculated from the entropy balance, Eq. (B.1) must be the same as calculated from the overall fluxes and forces, Eq. (B.2).

$$\sigma_{balance}^{tot} = \left(\frac{J'_{q,n}}{T_{out}} - \frac{J'_{q,1}}{T_{in}} \right) + (S_{w,n}(T_i) - S_{w,1}(T_i))J_w \quad (B.1)$$

$$\sigma_{JX}^{tot} = \Delta_{in} \left(\frac{1}{T} \right) J'_{q,n} - \frac{\Delta_{in} \mu_w(T_i)}{T_i} J_w \quad (B.2)$$

The equations express the entropy production accumulated until volume no n. For the whole system, this amounts to.

$$\sigma_{n_1}^{tot} = \sigma_{n_1}^{SJ} + \sum_{k=2}^{n-2} \sigma_{n_1,k}^h + \sigma_{n_1}^{SI} \quad (B.3)$$

$$\sigma_T^{tot} = \sigma_T^{SJ} + \sum_{k=1}^{n-2} \sigma_{T,k}^h + \sigma_T^{SI} \quad (B.4)$$

2. The local entropy production. The local entropy production is everywhere non-negative, meaning that:

$$\sigma = \sum_{i=1}^n J_i X_i \geq 0 \quad (B.5)$$

The fluxes and driving forces refer here to the control volume in question.

3. The overall driving forces. The thermal and chemical driving forces across a control volume must add to the overall driving forces over the membrane. The thermal driving forces are calculated from Eqs. (B.6) to (B.8). Points a and b indicate the left and right side, respectively, of a CV.

$$\Delta_{in} \frac{1}{T} = \frac{1}{T_n} - \frac{1}{T_1} \quad (B.6)$$

$$\Delta_{in} \frac{1}{T} = r_{qq}^{tot} J_{q,n}' + r_{qw}^{tot} J_w \quad (B.7)$$

$$\Delta_{in} \frac{1}{T} = \sum_{k=1}^{n-1} \Delta_{ab}^k \frac{1}{T} \quad (B.8)$$

The total chemical driving force over the membrane is calculated from Eq. (5). It must be equal to the sum of the local chemical driving forces of all CV's calculated from the proper resistivities and fluxes. The chemical potential difference is calculated at constant temperature T_1 .

$$-\frac{\Delta_{in} \mu_w(T_i)}{T_i} = -\frac{\mu_{w,n}(T_i) - \mu_{w,1}(T_i)}{T_i} \quad (B.9)$$

$$-\frac{\Delta_{in} \mu_w(T_i)}{T_i} = r_{wq}^{tot} J_{q,n}' + r_{wt}^{tot} J_w \quad (B.10)$$

$$-\frac{\Delta_{in} \mu_w(T_i)}{T_i} = \sum_{k=1}^{n-1} -\frac{\Delta_{ab}^k \mu_w(T_i)}{T_i} \quad (B.11)$$

4. The resistivity coefficients. The resistivity matrix on any level of description must obey the Onsager relations and have a positive definite determinant [13].

$$r_{qw} = r_{wq} r_{qq} r_{ww} - r_{qw} r_{wq} \geq 0 \quad (B.12)$$

References

- [1] U. Nations, International decade for action 'Water for Life' 2005 – 2015, 2014. (<http://www.un.org/waterforlifedecade/scarcity.shtml>),
- [2] USGS, USGS Water science school, 2014. (<http://water.usgs.gov/edu/earthwherewater.html>),
- [3] A. Jansen, J. Assink, J. Hanemaaijer, J. van Medervoort, E. van Sonsbeek, Development and pilot testing of full-scale membrane distillation modules for deployment of waste heat, *Desalination* 323 (2013) 55–65.
- [4] M. Findley, Vaporization through porous membranes, *Ind. Eng. Chem. Process Des. Dev.* 6 (2) (1967) 226–230.
- [5] J. Hanemaaijer, J. van Heuven, Method for the purification of a liquid by membrane distillation, in particular for the production of desalinated water from seawater or brackish water or process water, (<http://www.google.com/patents/EP1185356A1?Cl=en>), eP Patent App. EP20,000,937,369, 2002.
- [6] J. Hanemaaijer, A. Jansen, J. van Medevoort, J. De, E. van Sonsbeek, E. Koele, J. Assink, Membrane distillation method for the purification of a liquid, (<http://www.google.com/patents/EP2094376A1?Cl=zh>), eP Patent App. EP20,070,834,654, 2009.
- [7] J. Hanemaaijer, A method of converting thermal energy into mechanical energy, and an apparatus therefore, (<http://www.google.com/patents/WO2012118369A3?Cl=en>), wO Patent App. PCT/NL2012/000,018, 2013.
- [8] N. Kuipers, J. Hanemaaijer, H. Brouwer, J. van Medervoort, A. Jansen, F. Altena, P. van der Vleuten, H. Bak, Simultaneous production of high-quality water and electrical power from aqueous feedstock's and waste heat by high-pressure membrane distillation, *Desalin. Water Treat.* 55 (2014) 2766–2776.
- [9] M. Khayet, T. Matsuura, *Membrane Distillation Principles and Applications*, Elsevier, 2011.
- [10] L. Martinez, F. Diaz, A. Hernandez, P. Pradanos, Characterisation of three hydrophobic porous membranes used in membrane distillation Modeling and evaluation of their water vapour permeabilities, *J. Membr. Sci.* 102 (2002) 15–27.
- [11] M. Gryta, M. Tomaszewska, Heat transport in the membrane distillation process, *J. Membr. Sci.* 144 (1998) 211–222.
- [12] G. Meindersma, C. Guijt, A. de Haan, Desalination and water recycling by air gap membrane distillation, *Desalination* 187 (2006) 291–301.
- [13] S. Kjelstrup, D. Bedeaux, *Non-equilibrium thermodynamics of heterogeneous systems*, Series on Advances in Statistical Mechanics - Volume 16, World Scientific Publishing Co., Singapore, 2008.
- [14] K. Lawson, D. Lloyd, *Membrane distillation*, *J. Membr. Sci.* 124 (1997) 1–25.
- [15] Ø. Wilhelmsen, T. Trinh, A. Lervik, V. Badam, S. Kjelstrup, D. Bedeaux, Coherent description of transport across the water interface: From nanodroplets to climate models, *Phys. Rev. E* 93, (<http://link.aps.org/doi/10.1103/PhysRevE.93.032801>).
- [16] L. Van der Ham, R. Bock, S. Kjelstrup, Modeling the coupled transfer of mass and thermal energy in the vapour-liquid region of a nitrogen-oxygen mixture, *Chem. Eng. Sci.* 65 (6) (2010) 2236–2248. <http://dx.doi.org/10.1016/j.ces.2009.12.021>.

- [17] L. Van der Ham, S. Kjelstrup, The importance of coupling between thermal and molar fluxes in a nitrogen oxygen distillation column, *IJoT* 14 (4).
- [18] D. Mendoza, S. Kjelstrup, Modeling a non-equilibrium distillation stage using irreversible thermodynamics, *Chem. Eng. Sci.* 66 (2011) 2713–2722.
- [19] J. Kuhn, R. Stemmer, F. Kapteijn, S. Kjelstrup, J. Gross, A non-equilibrium thermodynamics approach to model mass and heat transport for water pervaporation through a zeolite membrane, *J. Membr. Sci.* 330 (2009) 388–398.
- [20] J. Villaluenga, S. Kjelstrup, A non-equilibrium thermodynamics model of multi-component mass and heat transport in pervaporation processes, *J. Non-Equil. Thermodyn.* 37 (2012) 353–376.
- [21] A. Basile, *Handbook of Membrane Reactors*, Woodhead Publishing, 2013.
- [22] J. Lee, T. Laou, R. Kamik, Nanofluidic transport governed by the liquid/vapour interface, *Nat. Nanotechnol.* 9 (2014) 317–323.
- [23] A. Burggraaf, L. Cot, *Fundamentals of Inorganic Membrane Science and Technology*, Elsevier, 1996.
- [24] P. Colonna, T. van der Stelt, *Fluidprop: A program for estimation of thermophysical properties of fluids*, URL (<http://www.FluidProp.com>), software, 2004.
- [25] L. Camacho, L. Dumeé, J. Zhang, J. Li, M. Duke, J. Gomez, S. Gray, Advances in membrane distillation for water desalination and purification applications, *Water* 5 (2013) 94–196.
- [26] M. Qtaishat, T. Matsuura, B. Krućek, M. Khayet, Heat and mass transfer analysis in direct contact membrane distillation, *Desalination* 219 (2008) 272–292.
- [27] R. Schofield, A. Fane, C. Fell, Gas and vapour transport through microporous membranes. II. Membrane distillation, *J. Membr. Sci.* 53 (1990) 173–185.